Precision Engineering 49 (2017) 262–277

Contents lists available at ScienceDirect

Precision Engineering

journal homepage: www.elsevier.com/locate/precision

Ultraprecision surface flattening of porous silicon by diamond turning

Mehdi Heidari, Jiwang Yan*

Department of Mechanical Engineering, Keio University, Hiyoshi 3-14-1, Kohoku-ku, Yokohama 223-8522, Japan

ARTICLE INFO

Article history:
Received 16 February 2017
Accepted 27 February 2017
Available online 1 March 2017

Keywords:
Porous material
Single-crystal silicon
Diamond turning
Material removal mechanism
Subsurface damage
Surface quality

ABSTRACT

Porous silicon is receiving increasing interest from a wide range of scientific and technological fields due to its excellent material properties. In this study, we attempted ultraprecision surface flattening of porous silicon by diamond turning and investigated the fundamental material removal mechanism. Scanning electron microscopy and laser Raman spectroscopy of the machined surface showed that the mechanisms of material deformation and phase transformation around the pores were greatly different from those of bulk single-crystal silicon. The mechanism of cutting was strongly dependent on the direction of cutting with respect to pore edge orientation. Crack propagation was dominant near specific pore edges due to the release of hydrostatic pressure that was essential for ductile machining. Wax was used as an infiltrant to coat the workpiece before machining, and it was found that the wax not only prevented chips from entering the pores, but also contributed to suppress brittle fractures around the pores. The machined surface showed a nanometric surface flatness with open pores, demonstrating the possibility of fabricating high-precision porous silicon components by diamond turning.

1. Introduction

Porous materials are a special class of engineering materials which are characterized by special properties such as high surface area, reduced volumetric density and increased permeability [1]. Silicon-based porous material is a very promising material due to its excellent physical and thermal properties, and compatibility with silicon-based microelectronics [2]. Porous silicon is a suitable dielectric material for its large surface area within a small volume, controllable pore sizes and active surface chemistry [3]. These features lead to interesting optical properties by mixing silicon with air in effective medium approximation. On the other hand, chemical and biological substances, cells and molecules are able to penetrate to the pores to change the performance of the original system. These excellent characteristics are driving force behind research into different applications of porous silicon such as optical sensing [4] and biomedical applications [5–7]. Recently, porous silicon has attracted great attention because of its applications in Li-ion batteries, owing to its high theoretical capacity. For example, a porous silicon electrode with Li22Si5 composition has a capacity of 4200 mAh/g, which is over 10 times that of an existing carbon anode [8,9]. Moreover, the application of porous silicon in solar cells is rapidly increasing as it has the capability of a wide absorption band and high transmission in a wavelength range from 700 to 1000 nm [10–12].

Porous silicon is prepared by anodization of a single-crystal silicon wafer, and needs to be manufactured into various shapes for solar cells and biomedical applications. Normally, the anodized porous silicon surface is uneven, which affects its performances in specific applications [12], thus needs to be flattened precisely. Conventionally, polishing has been used for smoothing a silicon wafer. However, it cannot be used for porous silicon because pores would be filled and closed by abrasives in the slurry during the polishing process. Face milling and peripheral grinding which were used for machining sintered titanium foams [13] are not suitable for porous silicon machining in terms of surface quality.

, was used in experiments. Fig. 3

Another alternative method is turning. There are a few reports on turning of porous metal materials. For example, the effects of tool geometry, tool material properties and machining parameters on the porosity of porous tungsten had been investigated by Chen et al. [14]. Schoop et al. [15] machined porous tungsten and tried to control brittle microfracture to obtain a suitable surface porosity. Pusavec [16] used a multi-objective optimization model based on genetic algorithms to achieve the best machining performance in cutting porous tungsten under cryogenic conditions by predicting the optimal input cutting parameters. In addition, in a previous study by the present authors, the possibility of turning porous carbon using a single-crystal diamond tool for direct fabrication of precision air bearing surfaces has been demonstrated [17].

* Corresponding author.
E-mail address: yan@mech.keio.ac.jp (J. Yan).

http://dx.doi.org/10.1016/j.precisioneng.2017.02.015
0141-6359/

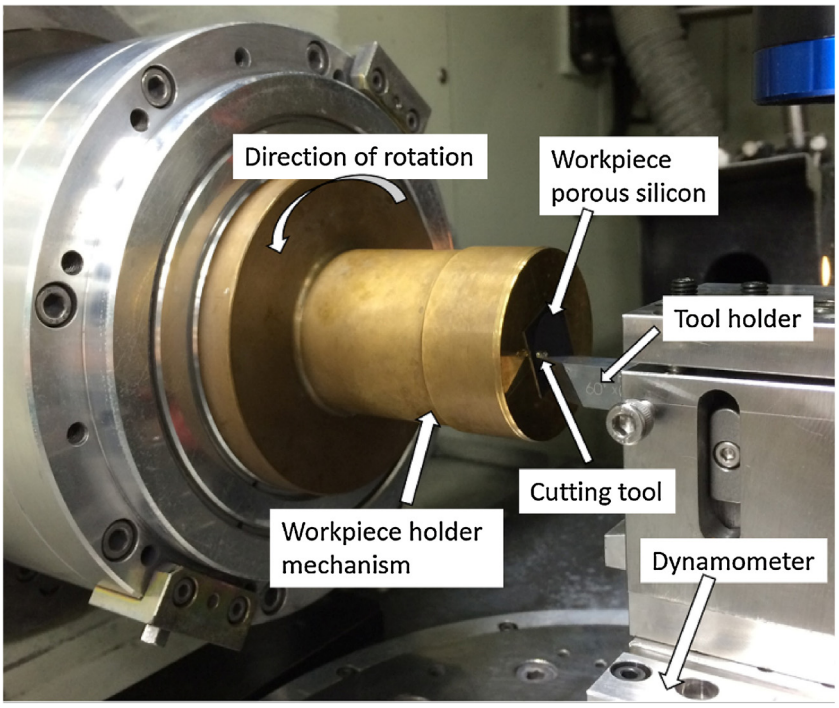

Fig. 1. Photograph of experimental setup.

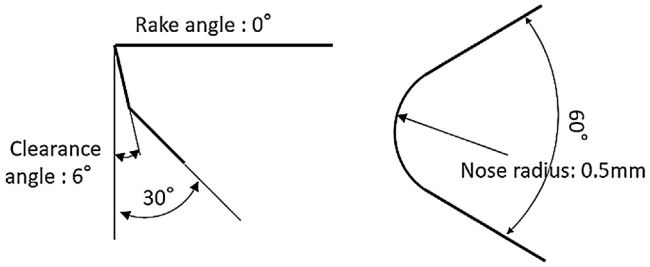

Fig. 2. Tool geometry.

However, to date, there is no available literature on the diamond turning of porous silicon. Silicon is a highly brittle material, thus its machining mechanism will be distinctly different from that of ductile metal materials. Especially, the micro pores in porous silicon will make the cutting process more complicated and difficult. In this study, diamond turning experiments of porous silicon have been performed to investigate the fundamental mechanisms of material removal and surface formation in order to realize ultraprecision flattening of the porous silicon surface.

2. Experimental procedures

2.1. Machining apparatus

Face turning was performed using a three-axis control ultraprecision machine, NACHI ASP-15 (NACHI-FUJIKOSHI CORP). A photograph of the main section of the machine is shown in Fig. 1. The machine has an ultraprecision air-bearing spindle, two perpendicular linear tables supported by high-stiffness hydrostatic bearings and driven by servomotors via hydrostatic screws with negligible mechanical friction, and a rotary table supported by hydrostatic bearings and driven by a friction drive in order to prevent from backlash movements. Laser hologram scales are used to accurately position all of these tables. Under precise numerical control, the linear tables can be moved at 1 nm per step and the rotary table can be rotated with an angular resolution of 0.00001°.

2.2. Diamond tool

A commercially available single-crystal diamond tool with a nose radius of 0.5 mm, rake and clearance angles of 0° and 6°, respectively, as shown in Fig. 2 shows a schematic model for diamond turning with a round-nosed tool, where the maximum undeformed chip thickness h_{max} is an important parameter to evaluate the cutting performance. h_{max} can be calculated from the tool nose radius R, depth of cut a and tool feed rate f, using the following equation when $f < \sqrt{2Ra - a^2}$ [18,19].

$$h_{max} = R - \sqrt{R^2 + f^2 - 2f\sqrt{2Ra - a^2}} \quad (1)$$

When $f \geq \sqrt{2Ra - a^2}$, however, h_{max} is equal to the depth of cut a. In this study, machining parameters were selected to make undeformed chip thickness range from ductile mode to brittle mode cutting for single crystal silicon.

2.3. Workpiece material

Two types of porous workpieces were used. One type had a thickness of 330 μm with blind pores and the other had a thick-

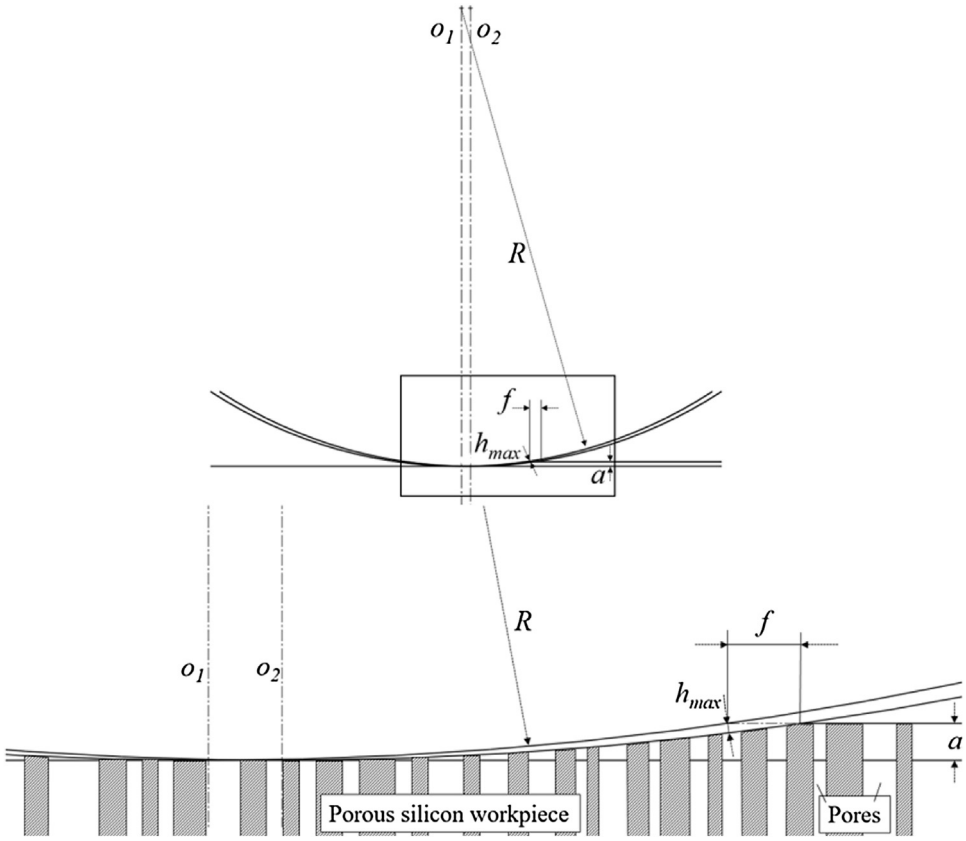

Fig. 3. Cutting model for porous silicon using a round-nosed tool.

ness of 260 μm with through pores. The workpiece size for both types is 20.0 mm × 20.0 mm with a porous zone of 16 mm in diameter and average pore size of 2.7 μm. Fig. 4 shows a photograph of a sample and an SEM micrograph of its surface. These porous silicon samples had been fabricated by anodic oxidation of single-crystal silicon (100) wafers. In addition to porous silicon samples, single-crystal silicon wafers (100) without pores were also machined in this study for comparison.

2.4. Machining conditions

Three circular areas, 1.5 mm in width for each, were cut on each sample at feed rates of 0.2, 2.0 and 10.0 μm/rev, as schematically shown in Fig. 5. Spindle rotation rate during cutting was fixed to 1500 rpm, consequently the cutting speed changed from 0.27 to 0.90 m/s. This range of cutting speed change is insufficient to cause remarkable difference in cutting behavior in terms of cutting forces and heat-induced material softening [20]. The depth of cut was ranged from 1 to 5 μm, and the actual depth of cut was measured from the uncut shoulder.

When cutting a porous material, cutting chips are easy to enter the pores, which might affect the surface function of the workpiece. In this work, to prevent chips from entering pores, wax was used in the experiments as pore infiltrant. The wax had a softening point of 76 °C and adhesion strength of 40 kg/cm^2. It was melted and then coated on the porous silicon surface (the through-hole type) so that it penetrated and filled completely the pores, as shown in Fig. 6. After machining, the wax was removed using ethanol and acetone compounds. Prior to machining, the sample was bonded onto a copper blank using a heat-softened wax and then vacuum chucked onto an air-bearing spindle.

2.5. Measurement apparatus

In order to evaluate the machined surface quality, a white light interferometer was used and the surface profile was analyzed by the Talymap software (Taylor Hobson Ltd.). A scanning electron microscope (SEM, Model Inspect S50) and a field-emission scanning electron microscope (FE-SEM, Model JSM-7600F, JEOL) were used to observe the sample surfaces and tool wear. A Laser micro-Raman spectroscope, NRS-2100 (JASCO Corp., Japan), was used to characterize the subsurface damage. In addition, a piezoelectric dynamometer (Kistler 9256C2) was mounted below the tool to measure micro-cutting forces during the cutting tests.

3. Results and discussion

3.1. Microfracture phenomena

Fig. 7a and b show SEM images of the machined surface of bulk single-crystal silicon without pores. As undeformed chip thickness was increased, the cutting mode transited from ductile to brittle. Microfractures began to form at an undeformed chip thickness between 248 nm to 532 nm, and the density of the microcracks increased with undeformed chip thickness. In contrast, Fig. 7c and d show SEM images for machined porous silicon. In this case, brittle mode machining is significant around pores while ductile mode machining was only observed in the areas among the pores. The size of brittle fractures increased with the increase of unreformed chip thickness.

Fig. 8 compares the surfaces machined at undeformed chip thickness of h_{max} = 122 and h_{max} = 532 nm at a higher magnification. At h_{max} = 122 nm, brittle fracture is mostly observed at pore

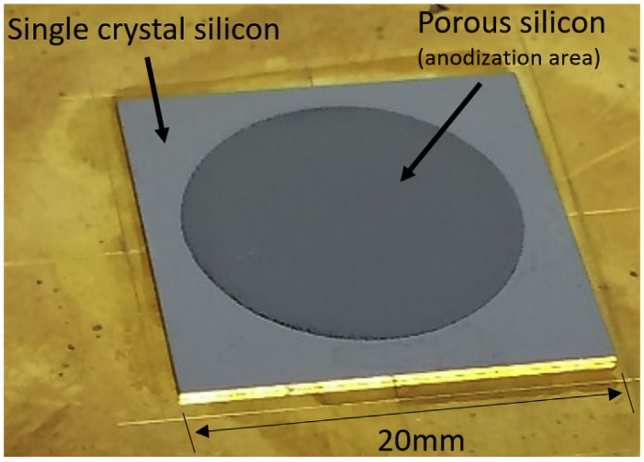

a)

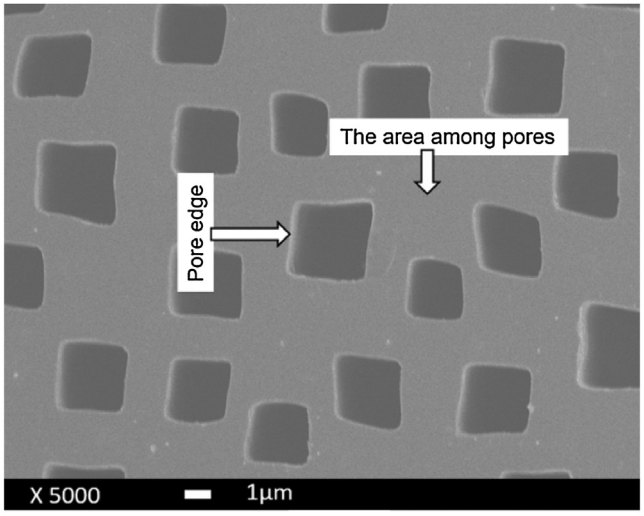

b)

Fig. 4. Porous silicon workpiece a) Overview photograph b) SEM micrograph of anodization area.

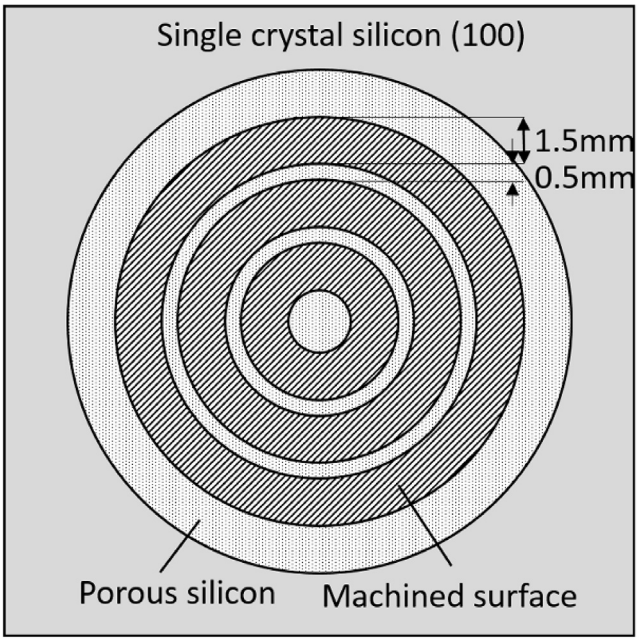

Fig. 5. Schematic illustration of machined areas on workpiece.

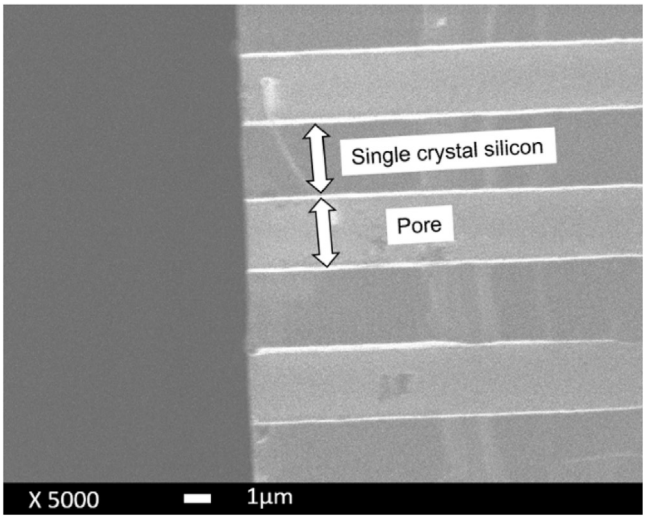

a)

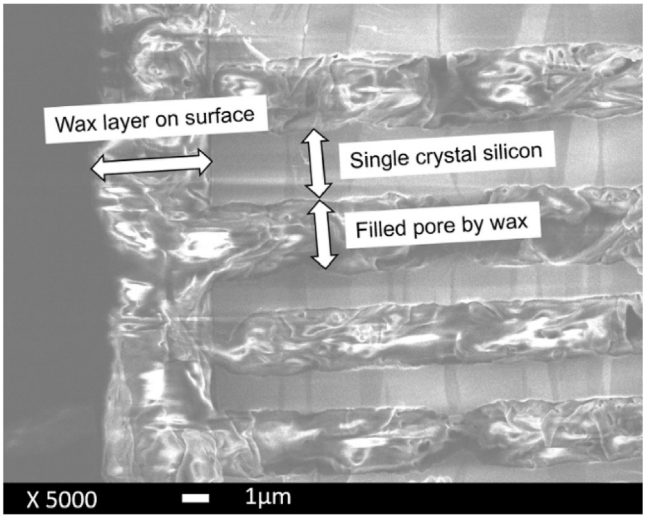

b)

Fig. 6. SEM micrographs of porous silicon cross sections showing pores before/after wax coating a) Before wax coating b) After wax coating.

edges, while by increasing h_{max} to 523 nm, the areas among pores are also fractured.

It is well-known that there is a brittle-ductile transition in chip formation during the cutting of brittle materials when the undeformed chip thickness is reduced [18,20–23]. When undeformed chip thickness is less than the critical undeformed chip thickness, no cracks are generated. When the undeformed chip thickness is larger than the critical value, however, microfractures are generated and the density of microfractures increases with the undeformed chip thickness.

Ductile mode cutting of a brittle material is based on hydrostatic pressure (compressive stress) which determines the extent of plastic deformation prior to fracture [24,25]. This stress state exists in the vicinity of cutting edge and is dependent on tool rake angle and undeformed chip thickness. When undeformed chip thickness becomes small enough, the entire cutting region will be under the high compressive stress state, such a high hydrostatic pressure becomes a prerequisite for machining brittle materials by plastic flow at room temperature [26]. In addition, high hydrostatic

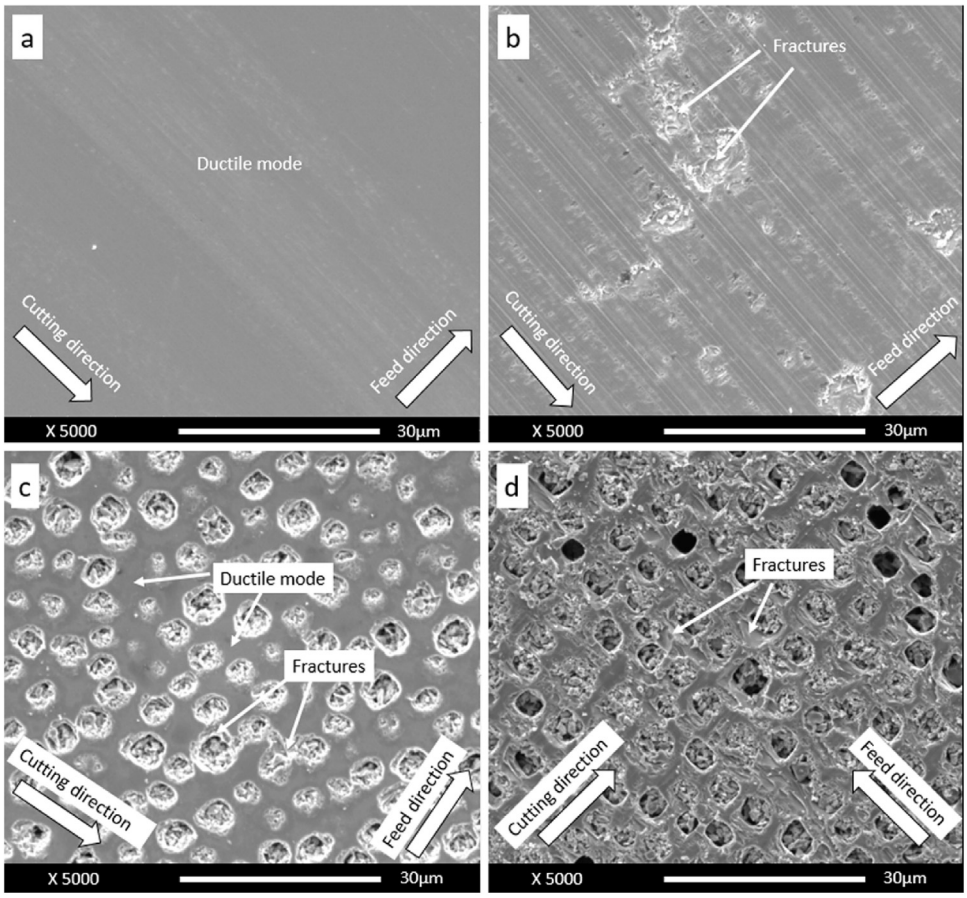

Fig. 7. SEM micrographs of machined surfaces of single-crystal silicon without pores and porous silicon at different undeformed chip thicknesses: (a, c) h_{max} = 12 nm, (b, d) h_{max} = 794 nm.

pressure can prevent microcrack propagation by closure of cracks [27].

Nevertheless, in a porous material, this kind of high hydrostatic pressure state cannot be maintained around a pore. This causes microcracks to propagate, and as soon as these cracks reach the pore walls, a part of silicon will be separated from the bulk, leaving fractures. To further investigate the phenomenon of material removal mechanism, the edges of a pore were divided into four groups according to the direction of cutting with respect to the orientation of a rectangular pore, as schematically shown in Fig. 9.

As shown in Fig. 10a, the area indicated by "I" was cut in a brittle mode, while the area indicated by "IV" was cut in a ductile mode. Both "II" and "III" areas were also cut in a brittle mode but less severely in comparison with the "I" area. The size of brittle fracture decreases with tool feed rate (Fig. 10b). Fig. 10c and d show pores having oblique edges to the cutting direction.

As shown in Fig. 11a, the area "I" is significantly influenced by the high-pressure induced by cutting edge, providing a condition for microcracks to propagate severely to reach the wall of pore because there is no resistance in the pore. When tool passes the pore, some chips are carried away by the rake face of the tool and some other chips would be pressed into the pore (Fig. 11b). As the tool reaches the "IV" area, as shown in Fig. 11c, the mechanism of cutting would be like that of a non-porous bulk material except that there is an impact from the tool to the pore edge.

The cutting mechanisms of the "II" and "III" areas involve brittle fractures too, but the size of brittle fractures depends on the relative position between the tool and the pore. When the tool feeds toward an edge of a pore, the tool feed-induced force has a significant side force component, as shown in Fig. 12a, which will lead to large brittle fractures around the pore edge. When the tool feeds over a pore, however, the side force component is vanishingly small, as shown in Fig. 12b, thus brittle fracture is greatly suppressed compared to that in Fig. 12a. From this meaning, it is presumable that using a tool with a larger nose radius can reduce the side force component.

SEM images of machined surface also indicated that as long as undeformed chip thickness was less than 248 nm, increasing depth of cut led to significant accumulation of chips in pores. As shown in Fig. 13, increasing depth of cut at the same feed rate results in higher material removal rate and consequently increases chip volume, and in turn, increased the chance for chips to enter pores.

3.2. Raman spectroscopy

It is known that for single-crystal silicon (c-Si), the triple degenerate optical phonons display in the first-order Raman spectrum a sharp peak at the Raman shift of 521 cm^{-1} and for amorphous silicon (a-Si), the first-order Raman spectrum reflects the phonon density of states and presents an optical band peak at 470 cm^{-1} [28,29]. To verify the microstructure of machined porous silicon surface, laser micro-Raman tests were performed on four areas of pores.

In Fig. 14, curve (I) shows the Raman spectrum of the surface machined at an undeformed chip thickness of 174 nm in "I" area of a pore. There is a characteristic Raman peak of c-Si at 521 cm^{-1}, whereas the intensity at other frequencies is negligibly low. This indicates that the subsurface layer is mainly crystalline silicon. Curves (II) and (III) show the Raman spectrum of the surface machined in the "II" and "III" areas, respectively, where the intensity of the Raman peak of c-Si at 521 cm^{-1} clearly becomes lower

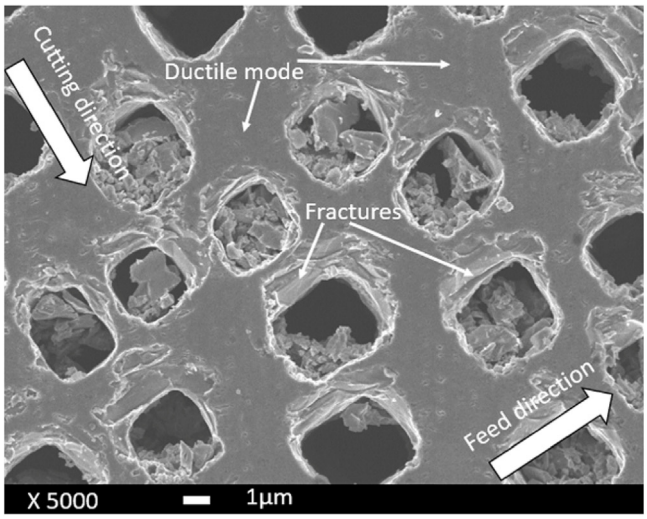

a)

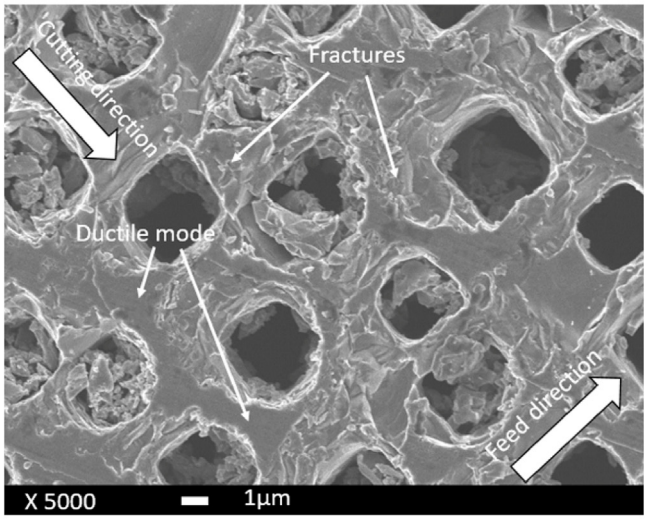

b)

Fig. 8. Magnified SEM micrographs of machined surface of porous silicon at different undeformed chip thicknesses a) h_{max} = 122 nm b) h_{max} = 532 nm.

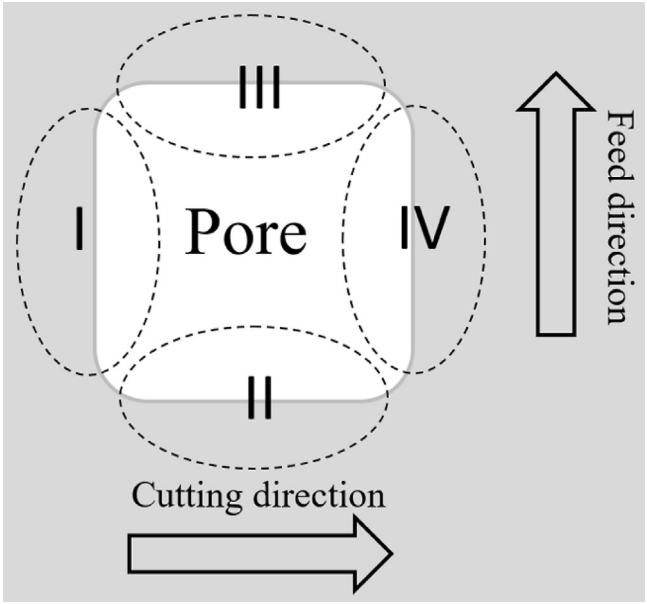

Fig. 9. Schematic illustrations of four areas of pore edges.

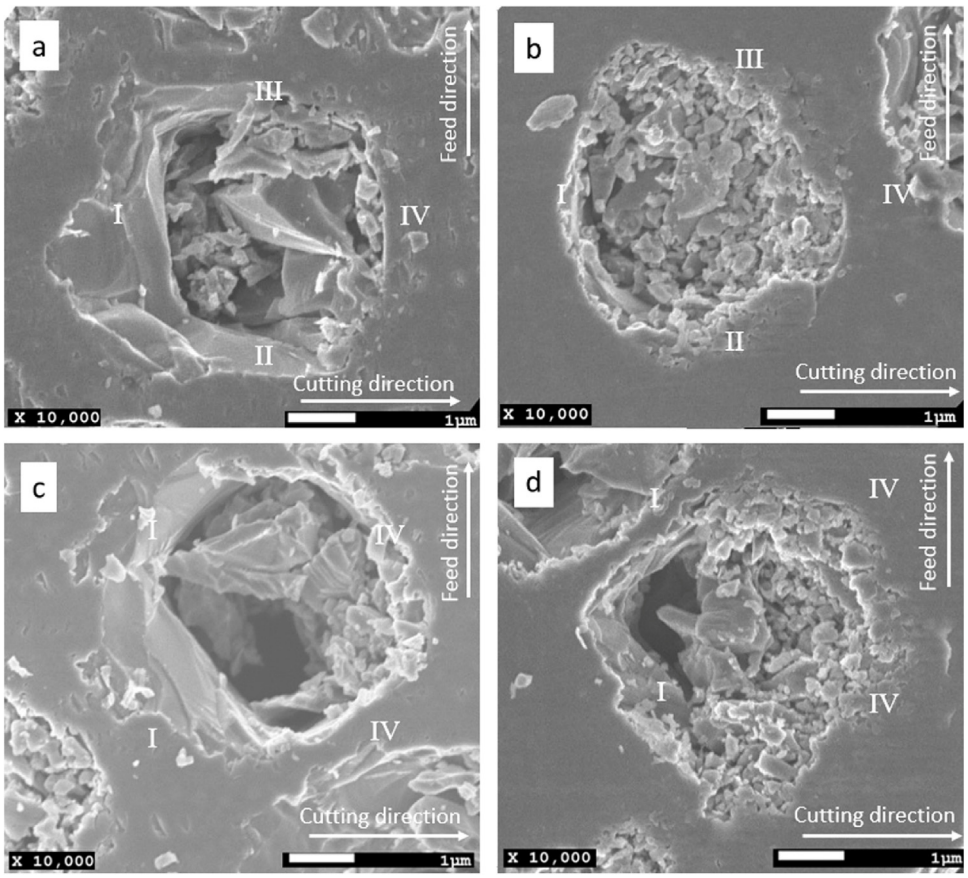

Fig. 10. Material removal behavior around pores: (a) h_{max} = 174 nm (f = 2.0 μm/rev, a = 2.0 μm); (b) h_{max} = 17 nm (f = 0.2 μm/rev, a = 2.0 μm); (c) h_{max} = 122 nm (f = 2.0 μm/rev, a = 1.0 μm); (d) h_{max} = 12.6 nm (f = 0.2 μm/rev, a = 1.0 μm).

than that in (I). However, a broadband peak centered at 470 cm^{-1} appears in (III), indicating that the subsurface layer has been partially transformed into an amorphous state. Curve (IV) shows the Raman spectrum of "IV" area of a pore. The broadband peak at 470 cm^{-1} becomes more significant, whereas a small peak can still be observed at 521 cm^{-1}. This indicates that the subsurface layer within the laser penetration depth has been mostly transformed into an amorphous state. This result is similar to that of machined bulk single crystal [28].

Raman spectra of the cutting chips were also investigated. Fig. 15a is the Raman spectrum of chips produced under the feed rate of 0.2 μm/rev, which shows a strong amorphous peak. In contrast, chips produced at a higher feed rate (f = 2.0 μm/rev) showed a combination of completely amorphous, partially amorphous, as well as crystalline phases, as shown in Fig. 15b.

3.3. Finite element simulation of stress distribution

To understand the change in cutting mechanisms around a pore, the cutting-induced stress distributions at the "I" and "IV" areas around a pore were investigated using AdvantEdge, a finite element machining simulation program produced by Third Wave Systems USA. The tool rake angle, relief angle and cutting speed used in the simulation were the same as those used in the experiments. The pressure-sensitive Drucker-Prager constitutive model [30–32] was used to establish the material property model for silicon. The main modeling parameters are shown in Table 1.

Fig. 16 shows stress distributions in the "I" and "IV" areas of a pore for an undeformed chip thickness of 532 nm. As the tool reaches the pore edge in the "I" area, as shown in Fig. 16a, a very large tensile stress area is formed beneath the tool tip and extending towards the pore. This kind of tensile stress induces microcrack propagation and results in brittle fractures [33,34]. In contrast, the stress distribution in the "IV" area is similar to that of bulk material cutting, where only an extremely small area beneath the tool tip is under tensile stress while the other areas are under compressive stress, as shown in Fig. 16b. There is a long area along the wall of the pore showing tensile stress, but the tensile stress is too low to cause brittle fractures. The simulation results agree well with the experimental results in 3.1 section, indicating that brittle fractures in the "I" area are more significant than those in the "IV" area.

Table 1
FEM modeling parameters.

Parameters	Value
Pressure-sensitivity coefficient	0.375
Material constant (GPa)	8.125
Hardness (GPa)	13.0
Tensile yield stress (GPa)	5.9
Young's modulus (GPa)	165

3.4. Effects of wax infiltrant

In order to prevent chips from filling pores during machining, wax was used as infiltrant in the next experiments. As shown in Fig. 17a, by using wax infiltrant and removing the wax after machining, chip-free pores were successfully obtained. Another noteworthy phenomenon in Fig. 17a is that there is almost no brittle fracture on the machined surface. Though the increase in undeformed chip thickness caused brittle fracture generation around

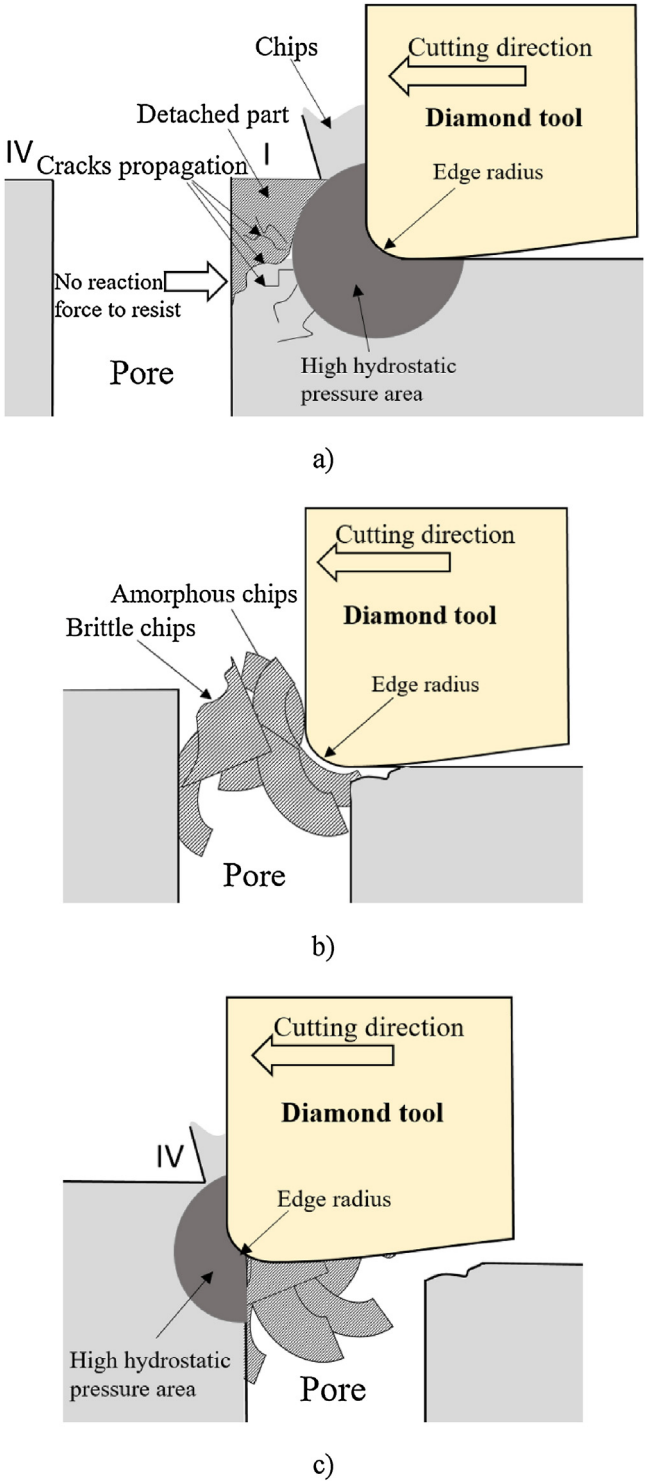

Fig. 11. Schematic illustrations of cutting mechanisms near a pore a) I area b) Pore area c) IV area.

pores (Fig. 17b–d), the brittle fractured areas are much smaller than that without wax infiltrant. In comparison to machining porous silicon without wax condition, using wax as infiltrant shows the significant improvement in the quality of machined surface. The use of wax as infiltrant might have two advantages. First, it prevents chips from getting into pores. Second, wax fully filling a pore can help to resist hydrostatic pressure around the pore to some extent, preventing the propagation of cracks.

Fig. 18 shows four different fracture patterns around pores observed at h_{max} = 25 nm. There are no chips in "IV" area thanks to the wax infiltrant. However, some chips are stuck on the "I" area in Fig. 18b and d. This might be a result of chip embedding into the wax inside the pores. Supported by the wax, the embedded chips are further cut and deformed by the subsequent tool pass, thus adhered onto the pore edges.

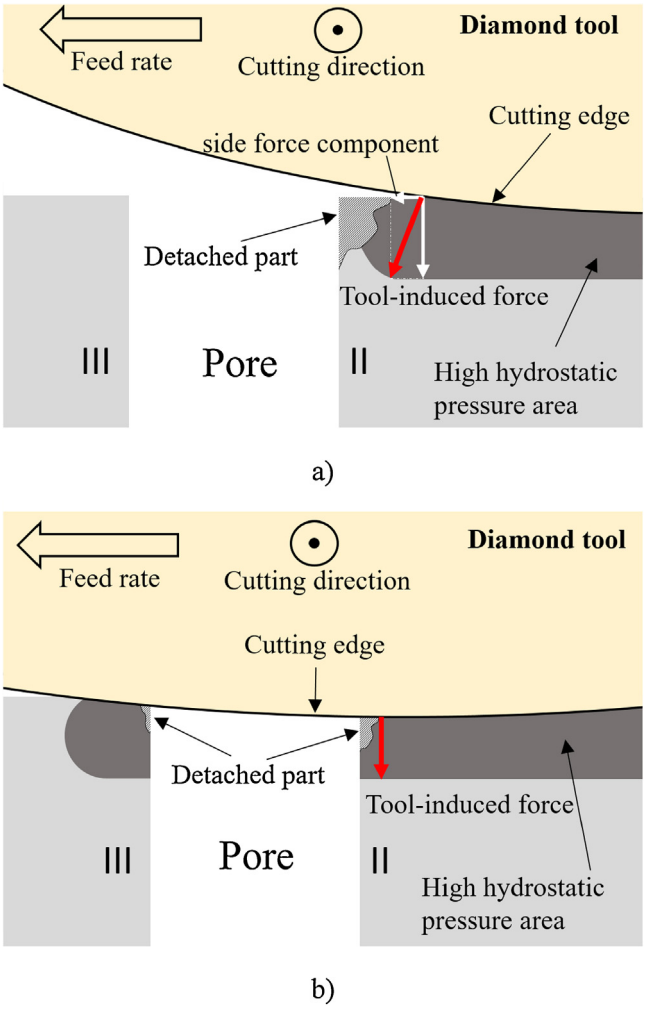

Fig. 12. Schematic illustrations of cutting mechanisms in II area and III area a) II area b) III area.

3.5. *Effects of tool chipping*

Fig. 19a is an SEM photograph of the tool edge after cutting of porous silicon for a total cutting distance of 105 m. The undeformed chip thickness was changed from 12.6 nm (f = 0.2 μm/rev, a = 1 μm) to 1163 nm (f = 10.0 μm/rev, a = 4 μm) during this cutting distance. In the figure, no obvious wear can be observed whereas a few micro-chippings have occurred to the edge. The size of these micro-chippings is approximately 1 μm. As cutting distance increased, both the number and the size of the micro-chippings increased. Fig. 19b is an SEM photograph of the cutting edge after a total cutting distance of 844m, where the size of micro-chippings ranged from 5 to 15 μm.

In ultraprecision cutting of bulk single-crystal silicon, there are two types of tool wear: micro-chippings and gradual wear [35]. The tool wear in ductile cutting is a stable and gradual process, where a slight crater wear and a significant flank wear occur. However, under brittle cutting mode, micro-chippings occur to the edge, which are caused by micro impacts from the craters on workpiece surface. Compared to bulk single-crystal silicon, the cutting mechanism of porous silicon involves numerous micro impacts from the pore edges. Thus, micro-chippings aggravate gradually, leading to bigger edge chippings. This situation is similar to the fracture of brittle-material tools in interrupted cutting or in the cutting of materials containing hard particles and inclusions [36,37].

Next, the effect of tool chipping on machined surface quality was examined. As shown in Fig. 20, using a chipped tool as shown

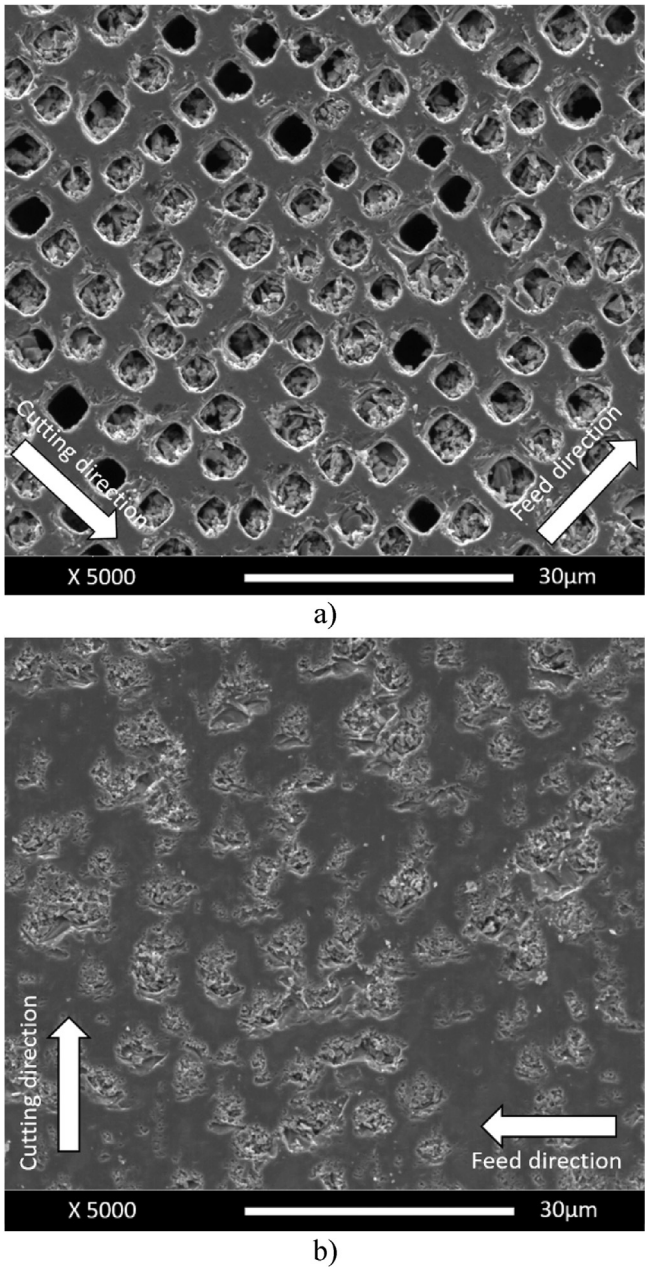

Fig. 13. SEM micrograph of surfaces machined at f = 2.0 μm/rev and different depth of cuts a) a = 1 μm b) a = 4 μm.

in Fig. 19b led to obvious brittle fractures around pores even at a very small undeformed chip thickness and even when using wax as infiltrant. As the size of tool micro-chippings (5–15 μm) is distinctly bigger than the depth of cut (1–5 μm), the tool will have a highly negative effective rake angle. In the cutting of non-porous silicon, a negative rake angle helps to generate hydrostatic pressure which makes brittle material deform in a plastic manner. In porous silicon cutting, however, the higher the hydrostatic pressure is, the severer the crack propagation around the pores when the high pressure is released around a pore. In addition, a highly negative rake angle pushes more chips inside the pores.

3.6. *Cutting force characteristics*

A comparison of cutting forces (principal forces) of bulk single-crystal silicon and porous silicon is plotted in Fig. 21. In the Fig., “a”, “b” and “c” indicate three stages of face turning: the stage of tool

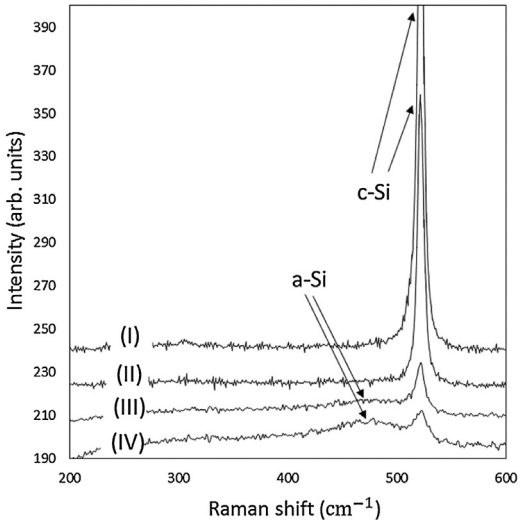

Fig. 14. Laser micro-Raman spectra of I, II, III and IV areas machined at h_{max} = 174 nm (f = 2.0 μm/rev, a = 2.0 μm).

approaching to workpiece, the steady cutting stage, and the stage of tool detaching from workpiece, respectively. Fig. 21 indicates that the magnitude of cutting force in machining of bulk single-crystal silicon is higher than that of porous silicon. This result might be attributed to two aspects: the low density of porous silicon, and the significant brittle fractures occurring around the pores.

To further investigate the major factor reducing the cutting force of porous silicon, the machining pressure induced by principal force was calculated using the chip cross section model in Fig. 22. The pressure was calculated from the principal force F and the contact area A_c perpendicular to the principal force F as

$$P = \frac{F}{A_c} \tag{2}$$

where F is derived from the experimentally measured principal force, and A_c is calculated by the following integral equation:

$$\begin{aligned} A_c &= \left(\int_{\frac{f}{2}}^{\sqrt{2Ra-a}} R - \sqrt{R^2 - x^2}\,dx \right) + (f \times a) - \left(\int_{\frac{f}{2}}^{\sqrt{2Ra-a}+f} - \sqrt{R^2 - (x-f)^2}\,dx \right) \\ &= \left[-\frac{1}{2}R^2 \left(arcsin\left(\frac{x}{R}\right) + \frac{1}{2} sin\left(2\ arcsin\left(\frac{x}{R}\right)\right)\right) + Rx + C_1 \right] + [f \times a] - \\ &\quad \left[-\frac{1}{2}R^2 \left(arcsin\left(\frac{x-f}{R}\right) + \frac{1}{2} sin\left(2\ arcsin\left(\frac{x-f}{R}\right)\right)\right) + R(x-f) + C_2 \right] \end{aligned} \tag{3}$$

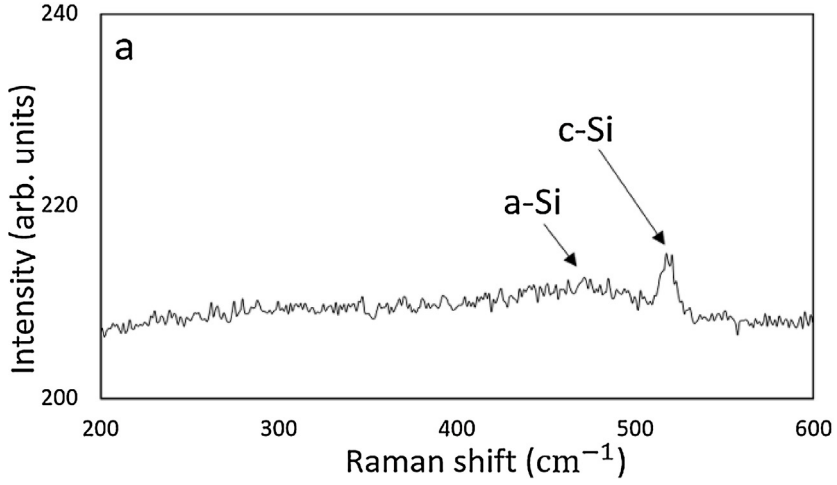

a)

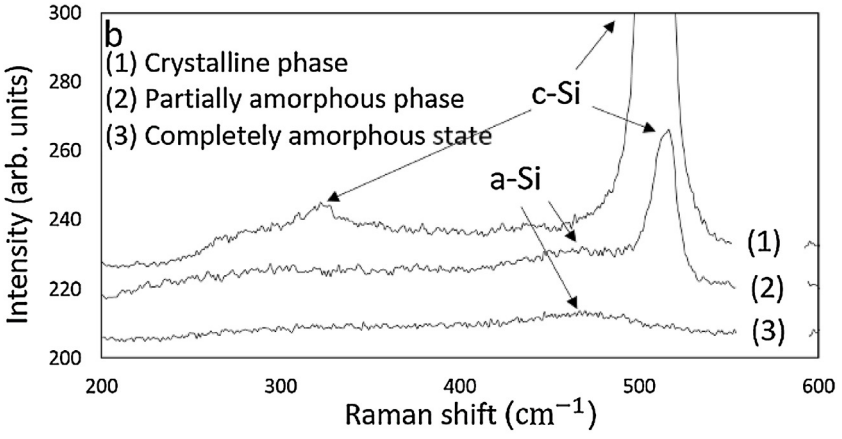

b)

Fig. 15. Laser micro-Raman spectra of chips in a pore a) f = 0.2 μm/rev, a = 1 μm b) f = 2.0 μm/rev, a = 1 μm.

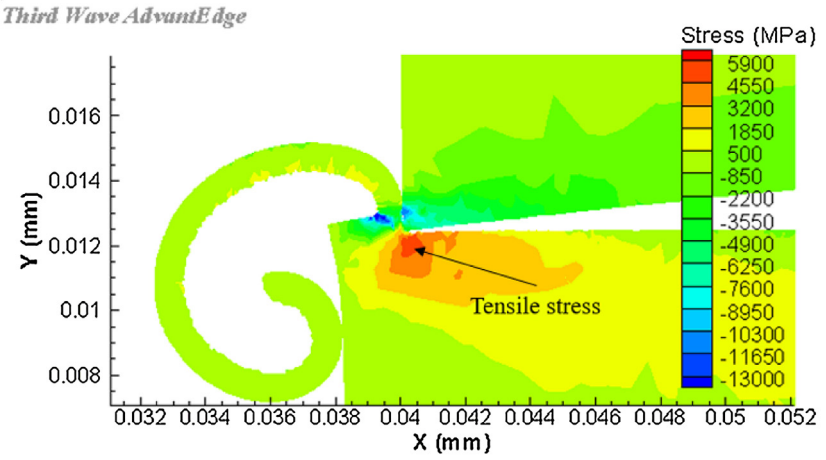

a)

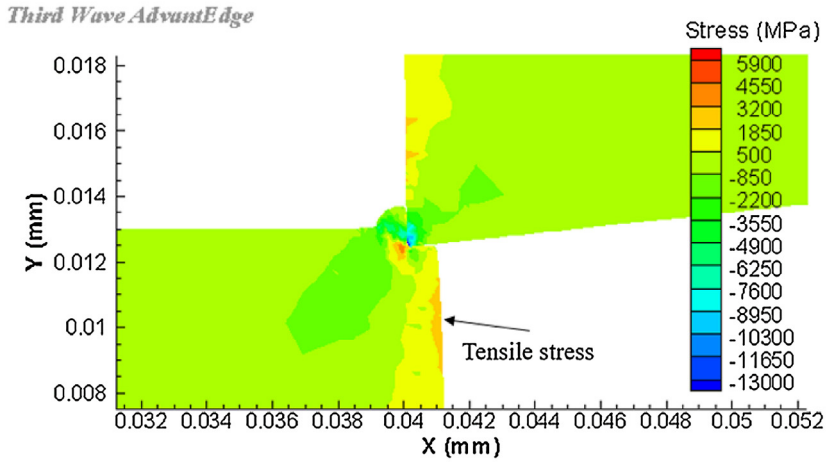

b)

Fig. 16. Stress distribution in the I and IV areas a) I area b) IV area.

When calculating the effective contact area between silicon and diamond, the porosity of the porous silicon workpiece was estimated by analyzing the SEM images of 10 different parts of the porous silicon surface using the ImageJ software. The results indicated that the surface porosity was approximately 30%. Therefore, the effective contact area between silicon and diamond was 0.7 times that of the cross sectional area of chip.

Table 2 shows the machining pressures in single-crystal silicon and porous silicon. The result reveals that the machining pressure decreases sharply with increasing tool feed rate. As the undeformed chip thickness increases, the principal force increase, but the slope of the force increase in the brittle region is remarkably smaller than that in the ductile region, because the brittle material removal results in lower cutting forces and subsequently less machining pressure [21,24]. From this meaning, it is presumable that the reduction of machining pressure in cutting porous silicon was mainly caused by the brittle fractures occurring around the pores.

It is also noted that using wax as infiltrant leads cutting force to increase. This increase can be accounted for the cutting resistance from the wax layer, which was about 30 μm thick above the porous silicon surface. In Fig. 21, the cutting forces between the third and fourth seconds were caused by the wax layer only.

3.7. Surface flatness

Surface flatness was measured in three-dimensional (3D) forms in which the average arithmetical deviation of area was calculated by using the TalyMap software. As the range of measurement of the white light interferometer was from −50 μm to 50 μm, it was not able to obtain data from the bottom of a pore. Thus, surface flatness measurement was based on the data obtained from areas among pores.

As shown in Fig. 23, the surface flatness of machined surface using wax infiltrant is better than that without wax and is almost the same as that of a single-crystal silicon wafer (flatness ranging from 8 to 13 nm) when undeformed chip thickness is $h_{max} < 25$ nm. Increasing undeformed chip thickness leads to worse surface flatness. Cutting porous silicon without wax infiltrant results in surface flatness between 80 nm to 180 nm. The surface flatness increases to ~500 nm when a chipped tool is used for cutting.

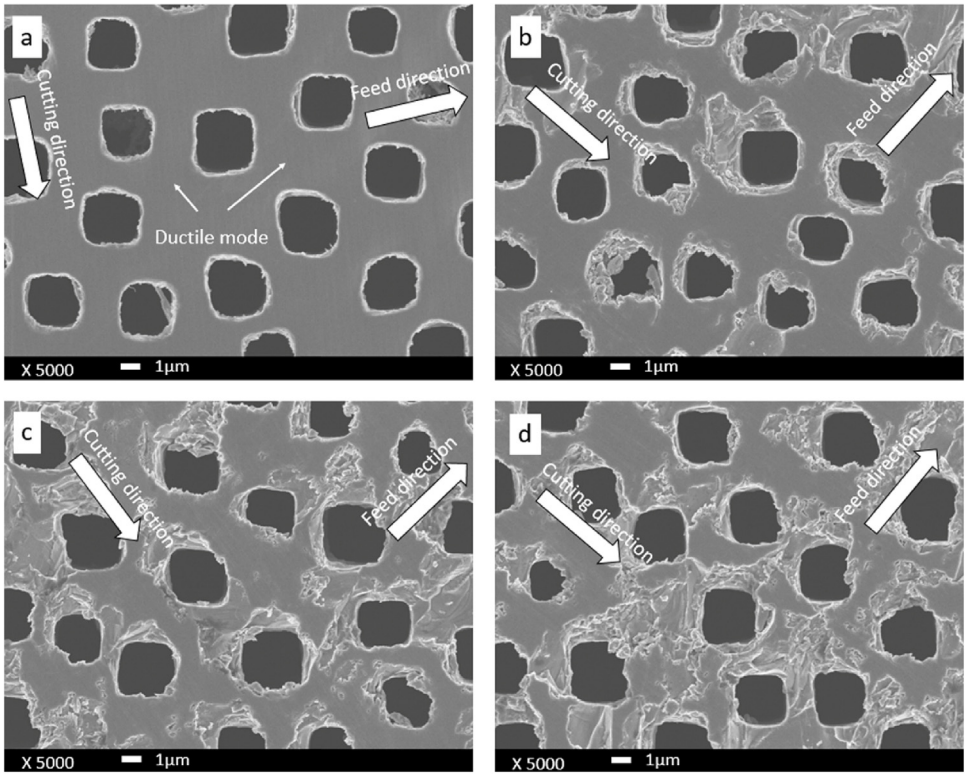

Fig. 17. SEM micrographs of surfaces machined using wax as infiltrant at different undeformed chip thicknesses: (a) h_{max} = 12 nm; (b) h_{max} = 286 nm; (c) h_{max} = 724 nm; (d) h_{max} = 1446 nm.

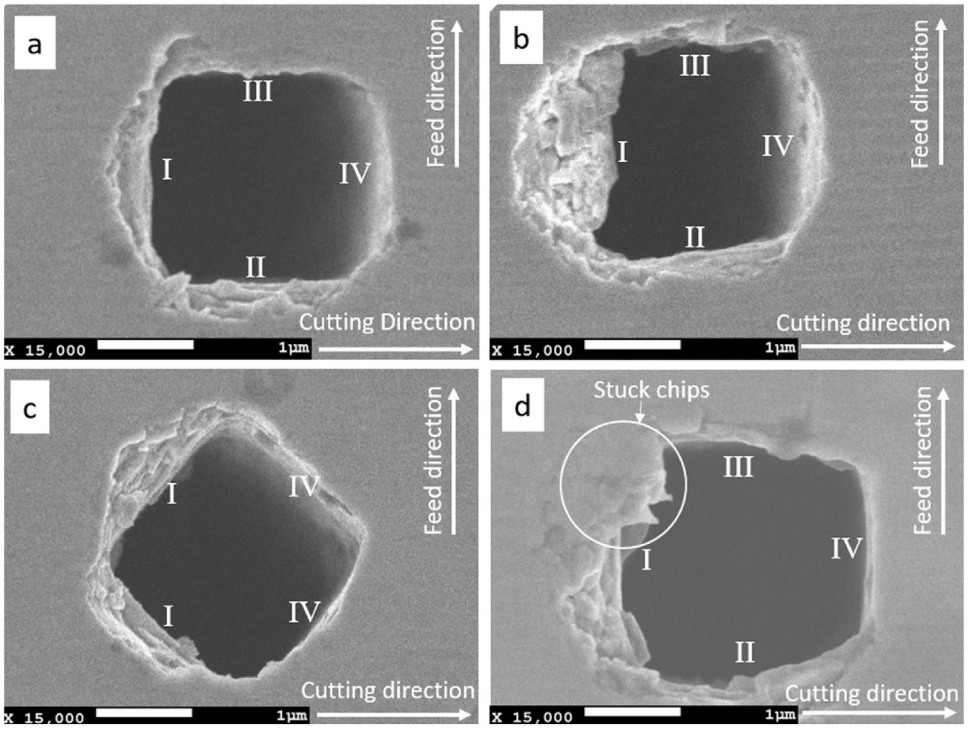

Fig. 18. Behavior of cutting in various pore areas when using wax (h_{max} = 25 nm).

Table 2
Machining pressure.

Workpiece material	f(μm/rev), a(μm)	A_c ($\times 10^{-12}$m^2)	F(N)	$P=F/A_c$ (GPa)
Single crystal silicon	$f=2.0$, $a=4$	7.9993	0.2861	35.76
	$f=10.0$, $a=4$	39.9167	0.4364	10.93
Porous silicon	$f=2.0$, $a=4$	0.7×7.9993	0.0802	14.32
	$f=10.0$, $a=4$	0.7×39.9167	0.1362	4.87

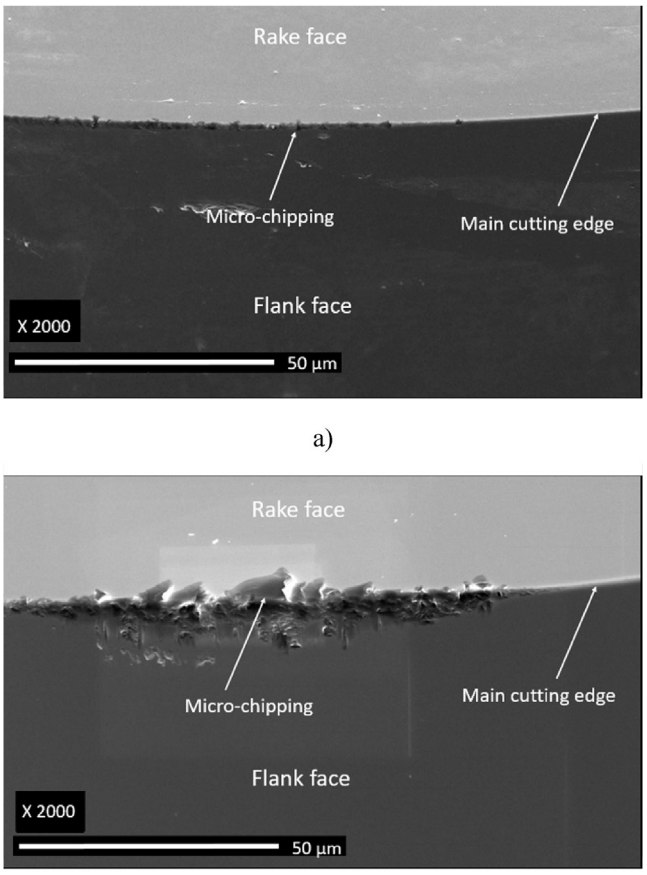

Fig. 19. SEM photographs of the cutting edge, showing occurrence of micro-chippings a) Cutting edge after cutting distance of 105 m b) Cutting edge after cutting distance of 844 m.

Fig. 24 shows 3D surface topographies of porous silicon before and after diamond turning. By applying wax as infiltrant and using a small undeformed chip thickness (h_{max} < 25 nm), high surface flatness is achieved. The surface flatness of the as-received porous silicon was 42 nm, while the one after diamond turning was 13 nm.

4. Conclusions

The fundamental material removal phenomena in diamond turning of porous silicon under various conditions were investigated experimentally. The following conclusions were drawn.

(1) The mechanism of cutting porous silicon is significantly different from that of bulk silicon due to existence of pores. The hydrostatic pressure induced by the cutting tool is released near the edge of a pore, causing microfractures.
(2) The mechanism of material removal is strongly dependent on the direction of cutting with respect to the pore edge orientation. Three types of material removal behaviors were confirmed in various areas around a pore: severely fractured area, slightly fractured area, and ductile-cut area.
(3) Raman spectroscopy showed that the material structures of subsurface layers of the above three kinds of areas are crystalline, partially amorphous, and completely amorphous, respectively.
(4) Cutting porous silicon using wax as infiltrant not only prevents chips from entering pores, but also shows significant improvement in surface quality in terms of decreasing brittle fractures.
(5) Micro-chippings of cutting edge occur, the number of size of which increases with total cutting distance. Tool chippings

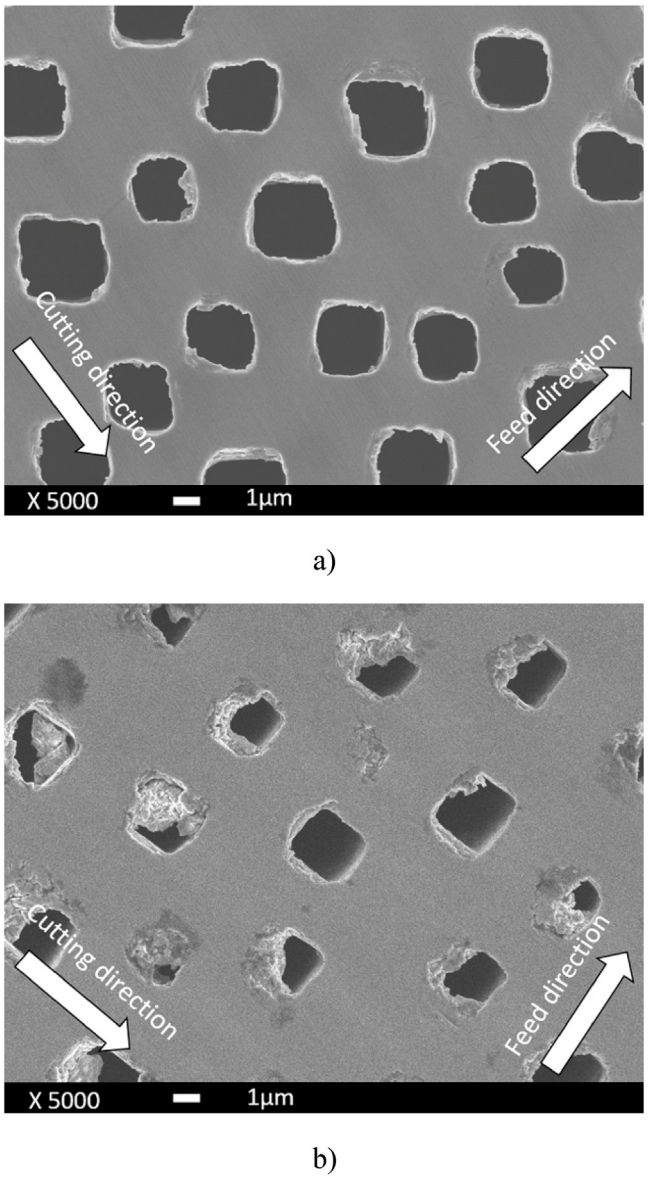

Fig. 20. Machined surface of porous silicon using (a) a new tool and (b) a chipped tool a) h_{max} = 19 nm b) h_{max} = 18 nm.

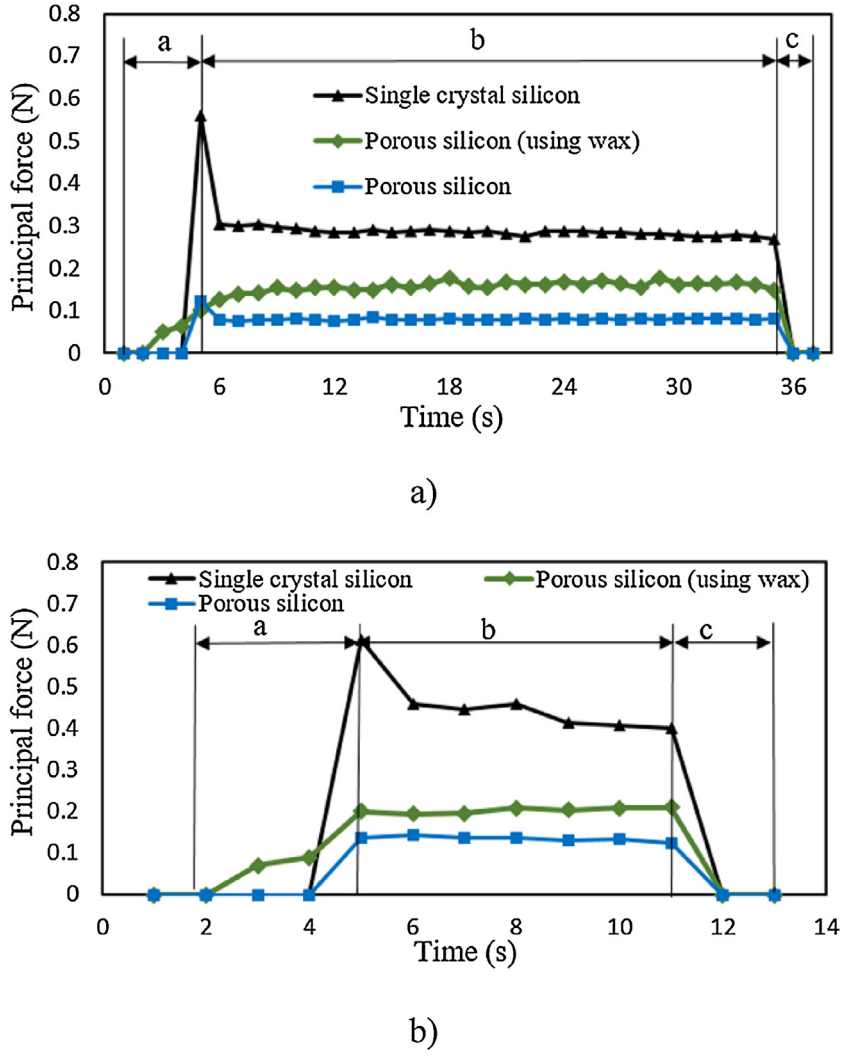

Fig. 21. Cutting force measurement results a) h_{max} = 248 nm (f = 2.0 μm/rev, a = 4 μm) b) h_{max} = 1163 nm (f = 10.0 μm/rev, a = 4 μm).

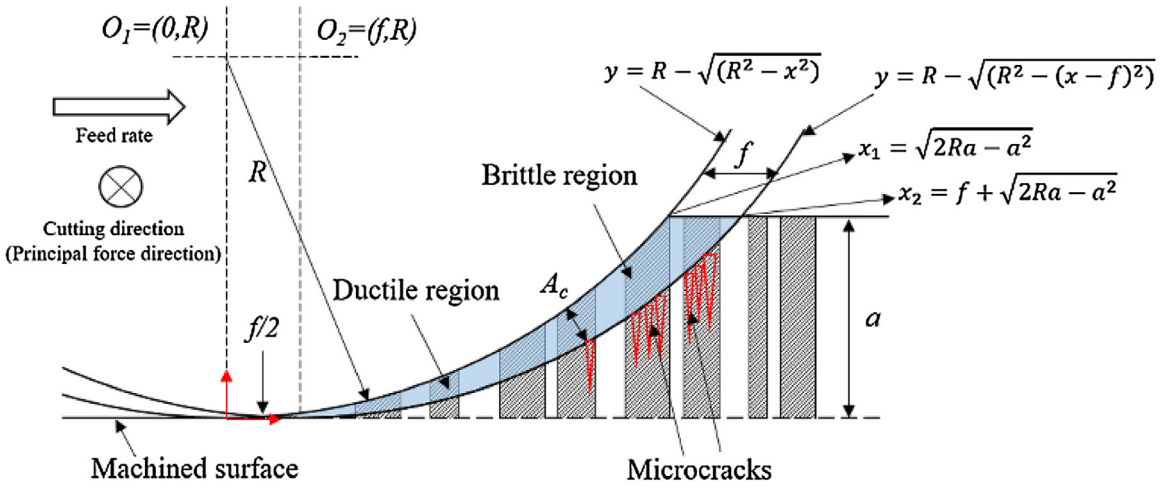

Fig. 22. Schematic model for undeformed chip cross section.

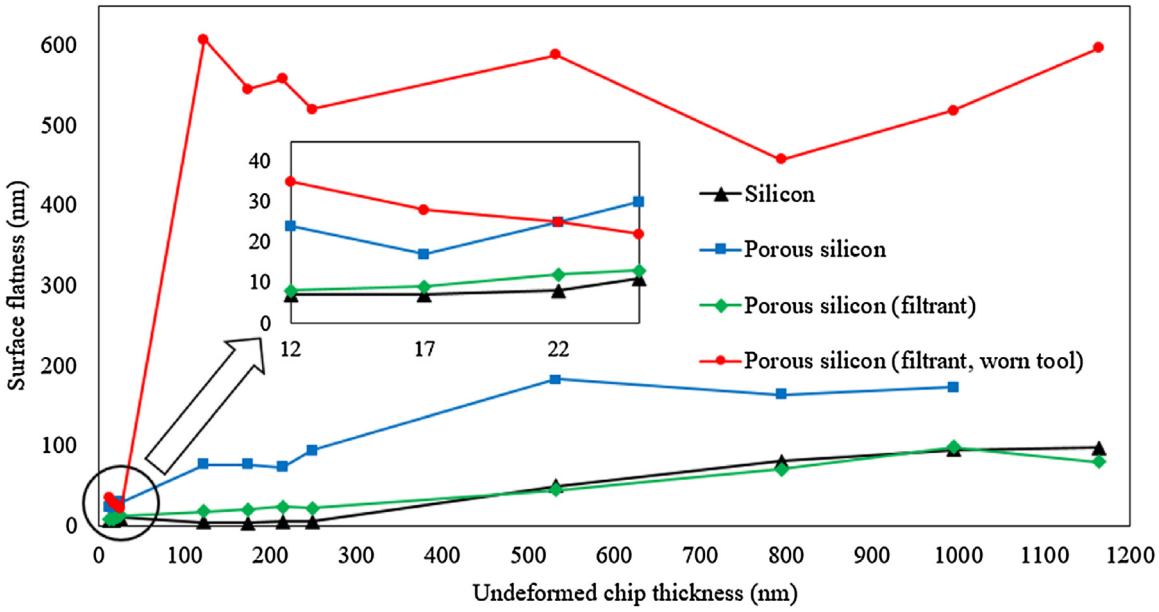

Fig. 23. Flatness of machined surfaces.

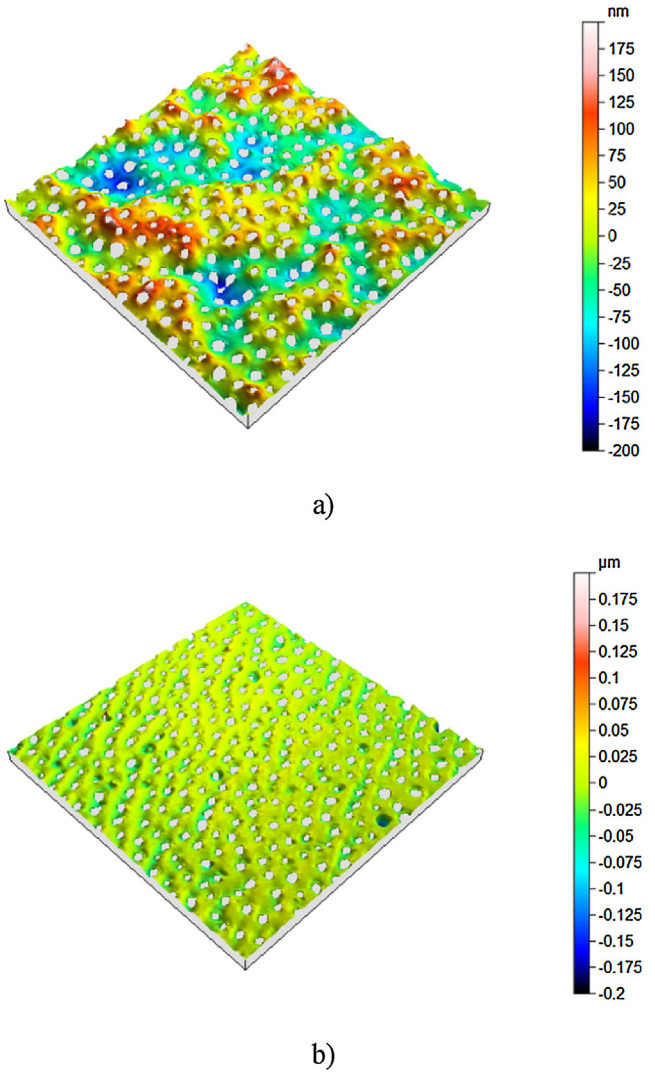

Fig. 24. 3D surface topographies of original porous silicon and machined one a) Original surface b) Machined surface.

cause a significant increase in micro fractures of silicon around pores.

(6) The cutting force in machining of porous silicon is remarkably lower than that of bulk single-crystal silicon due to the brittle fractures around pores and the low density of porous silicon.

(7) The surface flatness of anodized porous silicon may be improved to the nanometric level by diamond turning.

The present study has demonstrated that by controlling cutting parameters and using wax as pore infiltrant, it is possible to obtain an extremely high surface flatness of porous silicon.

References

[1] Tutunea-Fatan OR, Fakhri MA, Bordatchev EV. Porosity and cutting forces: from macroscale to microscale machining correlations. Proc Inst Mech Eng Part B J Eng Manuf 2011;225:619–30.
[2] Hirschman KD, Tsybeskov L, Duttagupta SP, Fauchet PM. Silicon-based visible light-emitting devices integrated into microelectronic circuits. Nature 1996;384:338–41.
[3] Striemer CC, Fauchet PM. Dynamic etching of silicon for broadband antireflection applications. Appl Phys Lett 2002;81:2980–2.
[4] Lin VS-Y, Motesharei K, Dancil K-PS, Sailor MJ, Ghadiri MR. A porous silicon-based optical interferometric biosensor. Science 1997;278:840–3 (80).
[5] Pérez EX. Design, fabrication and characterization of porous silicon multilayer optical devices. Universitat Rovira i Virgili; 2007.
[6] Chan S, Fauchet PM, Li Y, Rothberg LJ, Miller BL. Porous silicon microcavities for biosensing applications. Phys Status Solidi Appl Res 2000;182:541–6.
[7] Föll H, Christophersen M, Carstensen J, Hasse G. Formation and application of porous silicon. Mater Sci Eng R Rep 2002;39:93–141.
[8] Gowda SR, Pushparaj V, Herle S, Girishkumar G, Gordon JG, Gullapalli H, et al. Three-dimensionally engineered porous silicon electrodes for Li ion batteries. Nano Lett 2012;12:6060–5.
[9] Thakur M, Isaacson M, Sinsabaugh SL, Wong MS, Biswal SL. Gold-coated porous silicon films as anodes for lithium ion batteries. J Power Sources 2012;205:426–32.
[10] Pacebutas V, Grigoras K, Krotkus A. Porous silicon applications in solar cell technology. Phys Scr 1997;T69:255–8.
[11] Canham LT. Silicon quantum wire array fabrication by electrochemical and chemical dissolution of wafers. Appl Phys Lett 1990;57:1046.
[12] Dubey RS. Electrochemical fabrication of porous silicon structures for solar cells. Nanosci Nanoeng 2013;1:36–40.
[13] Bram M, Kempmann C, Laptev A, Stöver D, Weinert K. Investigations on the machining of sintered titanium foams utilizing face milling and peripheral grinding. Adv Eng Mater 2003;5:441–7.
[14] Chen S, Head D, Jawahir IS. An investigation of machining performance for controlled surface quality requirements in porous tungsten [for dispenser cathodes]. Fifth IEEE Int. Vac. Electron. Conf., vol. 52. 2004. p. 358–9 (IEEE Cat. No.04EX786).

[15] Schoop J, Effgen M, Balk TJ, Jawahir IS. Improved product quality and resource efficiency in porous tungsten machining for dispenser cathode application by elimination of the infiltration process. In: Nee AYC, Song B, Ong S-K, editors. Re-engineering Manuf. Sustain. Proc. 20th CIRP Int. Conf. Life Cycle Eng. Singapore 17–19 April 2013. Singapore: Springer Singapore; 2013. p. 241–4.
[16] Pusavec F. Porous tungsten machining under cryogenic conditions. Int J Refract Met Hard Mater 2012;35:84–9.
[17] Heidari M, Yan J. Investigation on surface formation mechanism of porous carbon in diamond turning. In: Proc. 8th Int. Conf. Lead. Edge Manuf. 21st Century, LEM 2015. 2015. p. 4–9.
[18] Yan J, Zhang Z, Kuriyagawa T. Mechanism for material removal in diamond turning of reaction-bonded silicon carbide. Int J Mach Tools Manuf 2009;49:366–74.
[19] Liu K, Li XP, Rahman M, Neo KS, Liu XD. A study of the effect of tool cutting edge radius on ductile cutting of silicon wafers. Int J Adv Manuf Technol 2007;32:631–7.
[20] Blake PN, Scattergood RO. Ductile-Regime machining of germanium and silicon. J Am Ceram Soc 1990;73:949–57.
[21] Yan J, Asami T, Harada H, Kuriyagawa T. Fundamental investigation of subsurface damage in single crystalline silicon caused by diamond machining. Precis Eng 2009;33:378–86.
[22] Shibata T, Fujii S, Makino E, Ikeda M. Ductile-regime turning mechanism of single-crystal silicon. Precis Eng 1996;18:129–37.
[23] Yan J, Asami T, Harada H, Kuriyagawa T. Crystallographic effect on subsurface damage formation in silicon microcutting. CIRP Ann Manuf Technol 2012;61:131–4.
[24] Patten J, Cherukuri H, Yan J. Ductile-regime machining of semiconductors and ceramics. In: Gogotsi Y, Domnich V, editors. High Press Surf. Sci. Eng. Taylor & Francis; 2003. p. 543–632.
[25] Yan J, Yoshino M, Kuriagawa T, Shirakashi T, Syoji K, Komanduri R. On the ductile machining of silicon for micro electro-mechanical systems (MEMS), opto-electronic and optical applications. Mater Sci Eng A 2001;297:230–4.
[26] Yan J, Syoji K, Kuriyagawa T, Suzuki H. Ductile regime turning at large tool feed. J Mater Process Technol 2002;121:363–72.
[27] Yoshino M, Aoki T, Shirakashi T, Komanduri R. Some experiments on the scratching of silicon:In situ scratching inside an SEM and scratching under high external hydrostatic pressures. Int J Mech Sci 2001;43:335–47.
[28] Yan J. Laser micro-Raman spectroscopy of single-point diamond machined silicon substrates. J Appl Phys 2004;95:2094–101.
[29] Gogotsi YG, Baek C, Kirscht F. Raman microspectroscopy study of processing-induced phase transformations and residual stress in silicon. Semicond Sci Technol 1999;14:936–44.
[30] Ajjarapu SK, Patten JA, Cherukuri H, Brand C. Numerical simulations of ductile regime machining of silicon nitride using the Drucker-Prager material model. Proc Inst Mech Eng Part C J Mech Eng Sci 2004;218:577–82.
[31] Patten JA, Jacob J, Bhattacharya B, Grevstad A, Fang N, Marsh ER. Numerical simulations and cutting experiments on single point diamond machining of semiconductors and ceramics. In: Yan J, Patten J, editors. Semicond. Mach. Micro-Nano Scale, vol. 661. Kerala, India: Transworld Research Network; 2007.
[32] Patten JA, Jacob J. Comparison between numerical simulations and experiments for single-point diamond turning of single-crystal silicon carbide. J Manuf Process 2008;10:28–33.
[33] Yang Y, De Munck K, Teixeira RC, Swinnen B, Verlinden B, De Wolf I. Process induced sub-surface damage in mechanically ground silicon wafers. Semicond Sci Technol 2008;23:75038.
[34] Boukharouba T, Elboujdaini M, Pluvinage G, editors. Damage and Fracture Mechanics. Dordrecht: Springer Netherlands; 2009.
[35] Yan J, Syoji K, Tamaki J. Some observations on the wear of diamond tools in ultra-precision cutting of single-crystal silicon. Wear 2003;255:1380–7.
[36] Wada R, Kodama H, Nakamura K, Mizutani Y, Shimura Y. Wear characteristics of single crystal diamond tool. CIRP Ann Manuf Technol 1980;29:47–52.
[37] Wong CJ. Fracture and wear of diamond cutting tools. J Eng Mater Technol 1981;103:341–5.